Chinese Journal of
POLYMER SCIENCE

RESEARCH ARTICLE

https://doi.org/10.1007/s10118-026-3772-9
Chinese J. Polym. Sci.

UiO-66-functionalized Sandwich Composite Separators for Improved Performance and Safety of Lithium-ion Batteries

Wen-Fei Ding[a,†], Yu-Xing Liu[a,†], and Lan Xu[a,b,c*]

[a] *National Engineering Laboratory for Modern Silk, College of Textile and Engineering, Soochow University, Suzhou 215123, China*
[b] *Jiangsu Engineering Research Center of Textile Dyeing and Printing for Energy Conservation, Discharge Reduction and Cleaner Production (ERC), Soochow University, Suzhou 215123, China*
[c] *Jiangsu Advanced Textile Engineering Technology Center, Nantong 226007, China*

Electronic Supplementary Information

Abstract Thermal runaway-induced safety issues have seriously hindered further development of lithium-ion batteries (LIBs). As a key component of LIBs, high-performance electrospun nanofiber separators (ENSs) with high-temperature self-closing functions can prevent safety issues caused by thermal runaway in LIBs. In this study, a sandwich-structured high-temperature self-closing polyacrylonitrile/polyurethane//adding cetyltrimethylammonium bromide to the poly(butylene succinate) (PAN/PU//CPBS) ENS (CPC ENS) was efficiently fabricated using free-surface electrospinning technology *via* material selection and structural design. A high-melting-point polyacrylonitrile-based ENS served as the intermediate layer, providing its thermal stability, while a low-melting-point polybutylene succinate-based ENS served as the outer layer, endowing it with a high-temperature self-closing function. To enhance its performance, CPC ENS was modified with polydopamine and loaded with porous structured UiO-66 rich in active sites, resulting in a high-performance self-closing UiO66@PDA@CPC ENS. The results showed that UiO66@PDA@CPC ENS had an excellent electrolyte uptake rate (740.7%±20.6%) and wettability (8.3°±0.3°), while maintaining good thermal stability at 160 °C. Furthermore, after 100 cycles at 0.5 C, the assembled battery maintained a discharge specific capacity of 139.6 mAh/g, with a capacity retention rate of 92.4%. Meanwhile, the surface of the lithium sheet had a flat morphology, indicating that UiO66@PDA@CPC ENS had superior long-term cycling stability, thus demonstrating its enormous potential as a high-performance and safe LIB separator.

Keywords Lithium-ion battery separator; Electrospinning; Nanofiber separator; Sandwich structure; Self-closing

Citation: Ding, W. F.; Liu, Y. X.; Xu L. UiO-66-functionalized sandwich composite separators for improved performance and safety of lithium-ion batteries. *Chinese J. Polym. Sci.* https://doi.org/10.1007/s10118-026-3772-9

INTRODUCTION

Lithium-ion batteries (LIBs) are widely used in electric vehicles, renewable energy storage, and portable electronic devices, owing to their high energy and power densities. They have become one of the leading representatives for storing renewable energy and are rapidly advancing toward higher energy densities and enhanced safety.[1–3] As critical components of LIBs, separators play a vital role in improving both safety and electrochemical performance.[4] Compared with commercial polyolefin separators, electrospun nanofiber separators (ENSs) with a three-dimensional network structure exhibit high porosity, excellent controllability, and large specific surface area. These properties facilitate electrolyte storage and Li-ion transport, enabling LIBs to be assembled with ENSs to demonstrate superior electrochemical performance.[5] However, safety issues caused by thermal runaway of LIBs remain an urgent problem. Overcharging, overheating, and electrolyte flammability can trigger thermal runaway in LIBs.[6,7] Therefore, designing ENSs with a high-temperature self-closing function is essential for preventing thermal runaway-induced safety issues in LIBs. They can immediately prevent electrochemical reactions from occurring when the internal battery temperature approaches thermal runaway thresholds, thereby deactivating the battery. Multilayer ENSs composed of materials with different melting points can achieve a high-temperature self-closing function by melting low-melting-point layers to seal pores while maintaining the original framework of high-melting-point layers.[8]

In our previous study,[9] a polyacrylonitrile/polyurethane (PAN/PU) ENSwith a mass ratio of 8:2 of polyacrylonitrile (PAN) and polyurethane (PU) was efficiently prepared using spherical section free-surface electrospinning (SSFSE), which exhibited excellent thermal stability under high-temperature conditions. However, this single-layer PAN/PU separator lacks thermoresponsive shutdown capability and fails to cut off battery operation under thermal abuse. The unmodified surface also constrains electrolyte wettability, ionic conductivity, and uniform Li^+ deposition regulation. Although multilayer

* Corresponding author, E-mail: lanxu@suda.edu.cn
† These authors contributed equally to this work.
Received April 10, 2026; Accepted June 5, 2026; Published online August 19, 2026

self-closing separators and metal-organic framework (MOF)-functionalized separators have been reported separately, few studies have combined multilayer construction, surface modification, and uniform MOF anchoring. This integrated strategy synergistically enables a controllable thermal shutdown, high thermal stability, superior electrolyte affinity, high Li^+ transference, and effective lithium dendrite suppression.

Polybutylene succinate (PBS), a biodegradable polyester, exhibits outstanding thermal stability, chemical resistance, and high toughness.[10,11] Crucially, its low melting point enables it to serve as a low-melting-point layer in multilayer ENSs, achieving the high-temperature self-closing function of ENSs by melting at high temperatures to block the pores.[4,12] Furthermore, adding cetyltrimethylammonium bromide (CTAB) to the PBS spinning solution can improve the PBS nanofiber morphology.[13–15] Therefore, this study efficiently fabricated a sandwich-structured high-temperature self-closing ENS using SSFSE, in which a high-melting-point PAN/PU was used as the intermediate layer to provide thermal stability, whereas a low-melting-point CTAB/PBS ENS (CPBS) was used as the outer layer to confer a high-temperature self-closing function, which could melt and block pores under high-temperature conditions. However, the poor thermal stability of CPBS would lead to a decrease in the thermal stability and electrochemical performance of CPBS/PAN/PU//CPBS (CPC) ENS. Accordingly, metal-organic frameworks (MOFs) with excellent thermal stability, porous structure, and abundant active sites are considered to enhance the thermal stability and electrochemical performance of CPC ENS.[16]

UiO-66 is a common MOF characterized by high specific surface area, abundant pore structure, good thermal stability, acid/alkali resistance, and diverse functional group modification capabilities.[17] Moreover, its open metal sites (OMSs) can synergistically release Li^+ with anions in the pore channels, enhancing the ion mobility.[16] Therefore, loading UiO-66 onto CPC ENS can effectively enhance the electrochemical performance and thermal stability of ENS. Among the various methods for compositing MOFs with fiber separators, dipping stands out as a preparation technique characterized by high loading capacity, simple experimental procedures, and material diversity.[18] Furthermore, studies indicate that the formation of a PDA layer on the fiber separator surface improves its thermal stability, mechanical properties, and electrochemical performance.[19–21] Concurrently, PDA exhibited excellent adhesion, with its abundant phenolic hydroxyl groups capable of bonding with the —COOH groups on UiO-66. Therefore, the CPC ENS was first treated with PDA to obtain an ENS with fibers uniformly wrapped in PDA (PDA@CPC). Subsequently, UiO-66 was loaded onto its surface to produce UiO66@PDA@CPC ENS. In this structure, UiO-66 was uniformly distributed on the ENS surface and within the fiber voids, providing favorable conditions for the stable shuttling and efficient transport of Li ions. In the current situation where self-closing separators suffer from insufficient electrochemical performance while high-performance separators exhibit poor safety,[7] the UiO66@PDA@CPC ENS has achieved a synergistic breakthrough of high safety and excellent electrochemical performance through material selection and structural design.

EXPERIMENTAL

The electronic supplementary information (ESI) detailed the raw material sources, together with the synthetic procedures of UiO-66, the fabrication of spinning solutions, the preparation of CPC ENS, and the formulation of UiO-66 dipping solutions. Additionally, the characterization and testing protocols for all as-prepared samples were fully provided therein.

Preparation of UiO66@PDA@CPC ENSs

As shown in Fig. 1, different spinning solutions were sequentially added to the reservoir of the SSFSE apparatus for electrospinning until the spinning solutions were exhausted, yielding CPC ENS. Subsequently, 2 mg/mL DA was added to a mixture of methanol and Tris-HCl buffer (50 mmol/L, pH=8.5) (1/1, *V*/*V*) and stirred thoroughly. CPC ENS was immersed in this mixture at room temperature for 6 h, and then removed and washed three times with deionized water before being dried in an oven to obtain PDA@CPC ENS. Similarly, PDA@CPC ENS was immersed in a

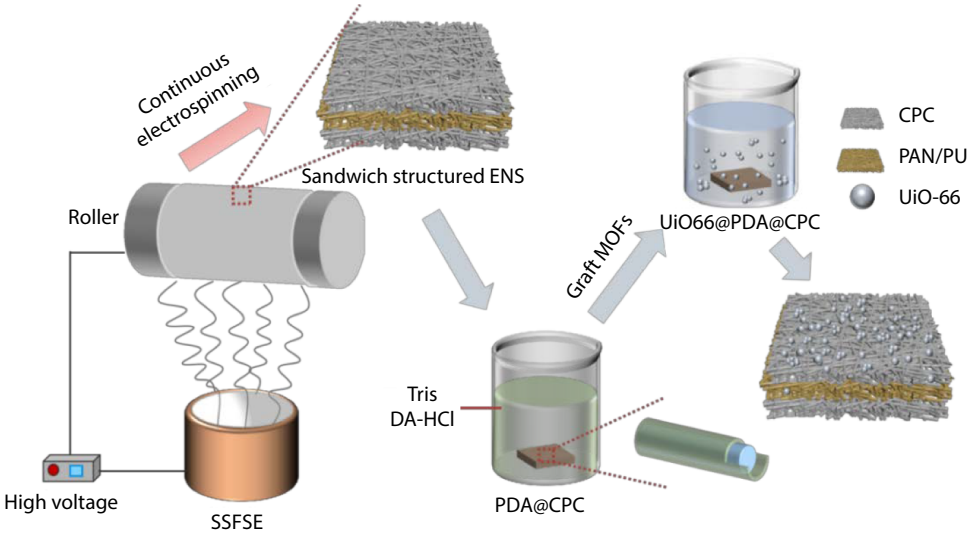

Fig. 1 Preparation diagram of UiO66@PDA@CPC ENS with a sandwich structure.

https://doi.org/10.1007/s10118-026-3772-9

dispersion prepared by uniformly dispersing 0.48 g UiO-66 in 80 mL of deionized water. After soaking at room temperature for 6 h, it was washed three times before being dried to obtain UiO66@PDA@CPC ENS. Additionally, CPC ENS were immersed in a UiO-66 loading solution and stirred at room temperature for 6 h before being removed. It was washed three times and finally dried to obtain the UiO66@CPC ENS as the control.

RESULTS AND ANALYSIS

Characterization of UiO-66

The SEM and TEM images of UiO-66 (Figs. 2a and 2b) show that the prepared UiO-66 nanoparticles exhibited regular octahedral shapes with uniform particle sizes (approximately 280 nm in diameter). Figs. S1(a) and S1(b) (in ESI) show the N_2 adsorption-desorption isotherm and pore size distribution of UiO-66. A typical Type I isotherm with negligible hysteresis was observed, confirming its microporous nature. UiO-66 delivered a high specific surface area of 1059.88 m^2/g, with pore size from 0.84–2.60 nm. Such a dominant microporous structure offered abundant sites for electrolyte adsorption and facilitated Li^+ transport in the ENS. To verify anion adsorption at the OMSs of UiO-66, Raman spectroscopy was conducted on the as-synthesized UiO-66 and the samples immersed in the electrolyte for 2 h. As shown in Fig. 2(c), new characteristic vibration peaks emerged at 600–1000 cm^{-1} in the Raman spectrum after electrolyte immersion, which were derived from the coordination bonding between PF_6^- anions and the coordinatively unsaturated Zr^{4+} OMSs of UiO-66. Meanwhile, the shift and distortion of the intrinsic framework peaks in UiO-66 demonstrated altered local coordination environments, confirming effective anion immobilization on OMSs. The elemental composition and valence states of UiO-66 were investigated using X-ray photoelectron spectroscopy (XPS). The full XPS spectrum (Fig. S1c in ESI) confirmed the presence of C, Zr, and O. The C 1s spectrum (Fig. 2d) was deconvoluted into three peaks, corresponding to C—C (284.73 eV), C—O (286.3 eV), and C=O (288.7 eV). The presence of these three types of bonds directly confirmed the complete retention of the BDC organic ligand in UiO-66. The Zr 3d spectrum (Fig. 2e) displays a characteristic doublet, which can be assigned to Zr $3d_{5/2}$ (183.11 eV) and Zr $3d_{3/2}$ (185.3 eV). The binding energies of these two peaks matched well with those of Zr^{4+} in ZrO_2, indicating that Zr in UiO-66 mainly existed in the +4 oxidation state. This is consistent with the typical coordination environment of Zr in the $Zr_6O_4(OH)_4$ secondary building units of the UiO-66 framework. Additionally, the O 1s spectrum (Fig. 2f) was fitted into three components corresponding to Zr—O (531.42 eV), C—O (532.6 eV), and O-metal (530) species. These XPS results confirm the successful synthesis of UiO-66 with abundant oxygen-containing functional groups.

Morphology and Characterization of ENSs

SEM images of PBS ENSs prepared from spinning solutions with different mass fractions of PBS are shown in Fig. S2 (in ESI), and the corresponding viscosity and conductivity of the spinning solutions are listed in Table S2 (in ESI). As the mass fraction of PBS increased, the solution viscosity continuously increased, but the conductivity exhibited a decreasing trend and was relatively low. Among them, the 10% PBS solution exhibited relatively moderate viscosity and conductivity, resulting in a comparatively favorable morphology of the PBS ENS prepared from it. To further enhance the morphology of the PBS ENSs, the cationic surfactant CTAB was added to the 10% PBS spinning solution to reduce its surface tension, making it easier for the jets to stretch and form fibers with smaller diameters and uniform distribution. As shown in Fig. S3 (in ESI), when CTAB added was 0.1 g, the CPBS spinning solution had relatively optimal viscosity and conductivity (Table S3 in ESI), resulting in the best morphology for the obtained CPBS ENS. This ENS featured the smallest fiber diameter (1065±88 nm) and the most uniform distribution, pro-

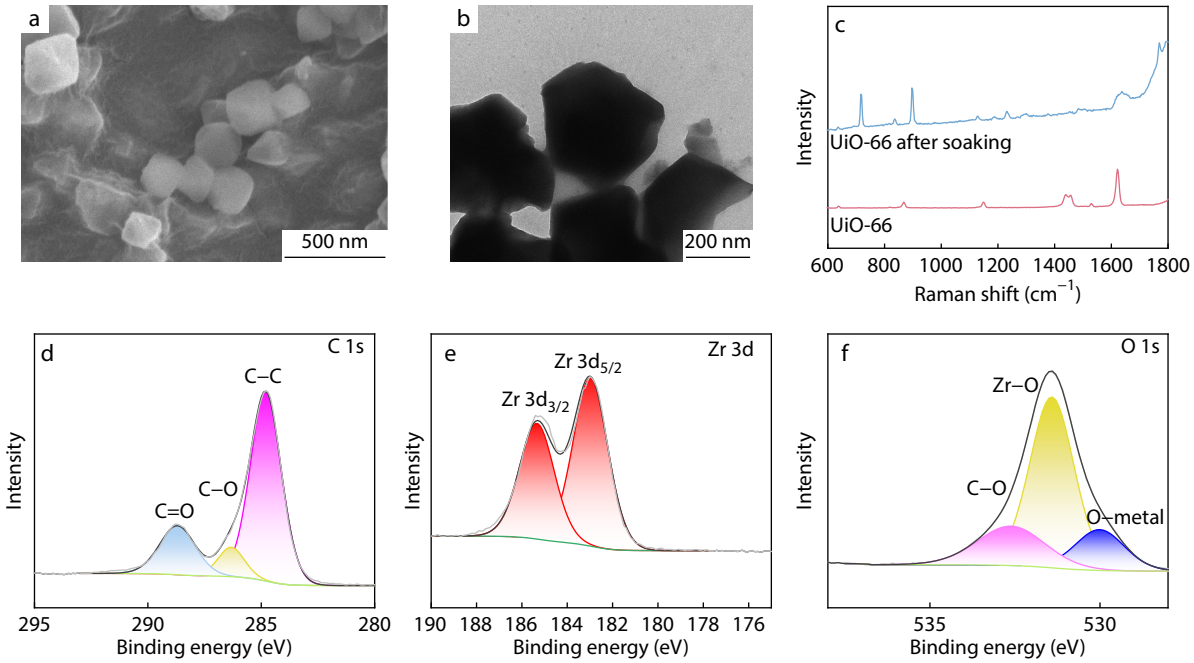

Fig. 2 (a) SEM and (b) TEM images of UiO-66; (c) Raman spectra of UiO-66; (d) C 1s, (e) Zr 3d and (f) O 1s XPS spectra of UiO-66.

https://doi.org/10.1007/s10118-026-3772-9

viding a solid foundation for uniform ion transport.

The SEM images of the CPC ENS (Figs. 3a and 3b) revealed their distinct sandwich structure. Fig. 3(c) indicates the agglomeration of UiO-66 particles within the UiO66@CPC ENS, resulting in a non-uniform particle distribution. Moreover, this agglomeration not only caused macroscopic thickness variations in the ENS but also induced significant local performance differences, thereby affecting the consistency of its overall performance.

As shown in Fig. 3(d), after immersing the CPC ENS in the DA solution, DA self-polymerizes on the nanofibers. The resulting PDA shell uniformly coated the CPBS nanofibers, with partial bonding occurring between the fibers (Fig. 3d), which enhanced the mechanical properties of the ENS. Furthermore, the magnified view revealed a relatively rough fiber surface (Fig. 3e). Fig. 3(f) shows that after loading UiO-66 onto the PDA@CPC ENS, UiO-66 was uniformly distributed on its fiber surface without agglomeration. This was primarily attributed to the interaction between the polar groups (*e.g.*, —OH) in the PDA shell and the —COOH groups of UiO-66, which not only enhanced the bonding strength between UiO-66 and the fiber surface but also promoted the uniform dispersion of particles. Simultaneously, the interconnected and tortuous pore structure effectively prevents lithium dendrite penetration, thereby mitigating internal short circuits and reducing self-discharge.[22,23]

Fig. 4(a) shows the infrared spectra of the different ENSs. It could be seen that PAN-2 exhibited absorption bands at 1730 and 2243 cm^{-1}, corresponding to the stretching vibration of the carbonyl group (—CO—) in RO—CO— and the stretching vibration of the cyano group (—CN—).[24] The bands appearing at 1228–1264 cm^{-1} in the ENSs containing CPBS were attributed to the stretching vibration of C—C—O in the ester group of PBS, while the bands at 1047 and 1714 cm^{-1} belong to the stretching vibration of O—C—C in PBS and the stretching vibration of the ester group (C≡O) in PBS, respectively.[25,26] The bands observed at 658 and 1575 cm^{-1} in UiO66@CPC and UiO66@PDA@CPC ENSs were attributed to the metal cluster (Zr–μ_3–O) and ligand (COO of BDC) in UiO-66, respectively, while the weak peak at 1505 cm^{-1} belonged to C=C vibrations.[27] Additionally, the peak observed at 1597 cm^{-1} in the UiO66@PDA@CPC ENS was attributed to the bending vibration of the-NH in PDA.[28,29] In summary, the FTIR results confirmed the successful preparation of UiO66@CPC and UiO66@PDA@CPC ENSs.[30] Fig. 4(b) shows the XRD patterns of different ENSs. The results indicated that ENSs containing CPBS exhibited characteristic peaks of PBS at 19.6° (020) and 22.5° (021).[31] The two sharp peaks observed at 7.4° (111) and 8.5° (200) in UiO66@CPC and UiO66@PDA@CPC ENSs were characteristic peaks of UiO-66, but no characteristic peaks of PBS appeared because UiO-66 covered the CPC ENS well.

Porosity has a significant impact on the electrochemical performance of the ENSs. A higher porosity enables ENSs to store more electrolytes, thereby enhancing their ionic conductivity.[32] The porosities of the different separators are shown in Fig. 4(c). The porosity of the PP separator was 33.6%±5.3%, while ENSs with a continuous pore structure significantly increased their porosity. Among them, the CPC ENS exhibited the highest porosity of 80.3%±7.4% because the composite of three-layer ENSs could provide more space for electrolyte storage, thereby enhancing the ionic conductivity of the ENS. The porosity of the UiO66@PDA@CPC ENS decreased to 51.9%±2.3%, which was similar to that of the UiO66@CPC ENS (50.5%±8.6%). This was because the loading of UiO-66 particles onto the CPC ENS caused partial pore blockage in the ENS, thereby affecting its porosity. However, compared to the PP separator, the UiO66@CPC ENS and UiO66@PDA@CPC ENS maintained sufficiently high porosities to ensure rapid Li^+ migration. Additionally, appropriate

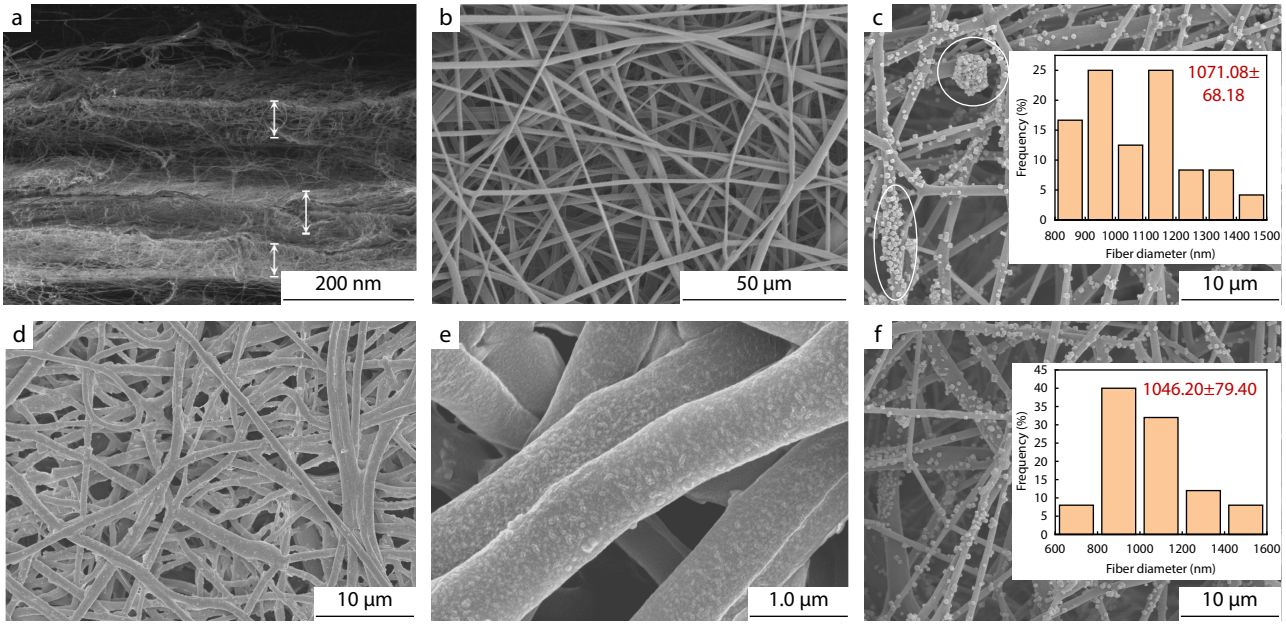

Fig. 3 (a) Cross-section and (b) top view SEM images of CPC ENS; (c) SEM image of UiO66@CPC ENS and its fiber diameter distribution; (d, e) SEM images of PDA@CPC ENS; (f) SEM image of UiO66@PDA@CPC ENS and its fiber diameter distribution.

https://doi.org/10.1007/s10118-026-3772-9

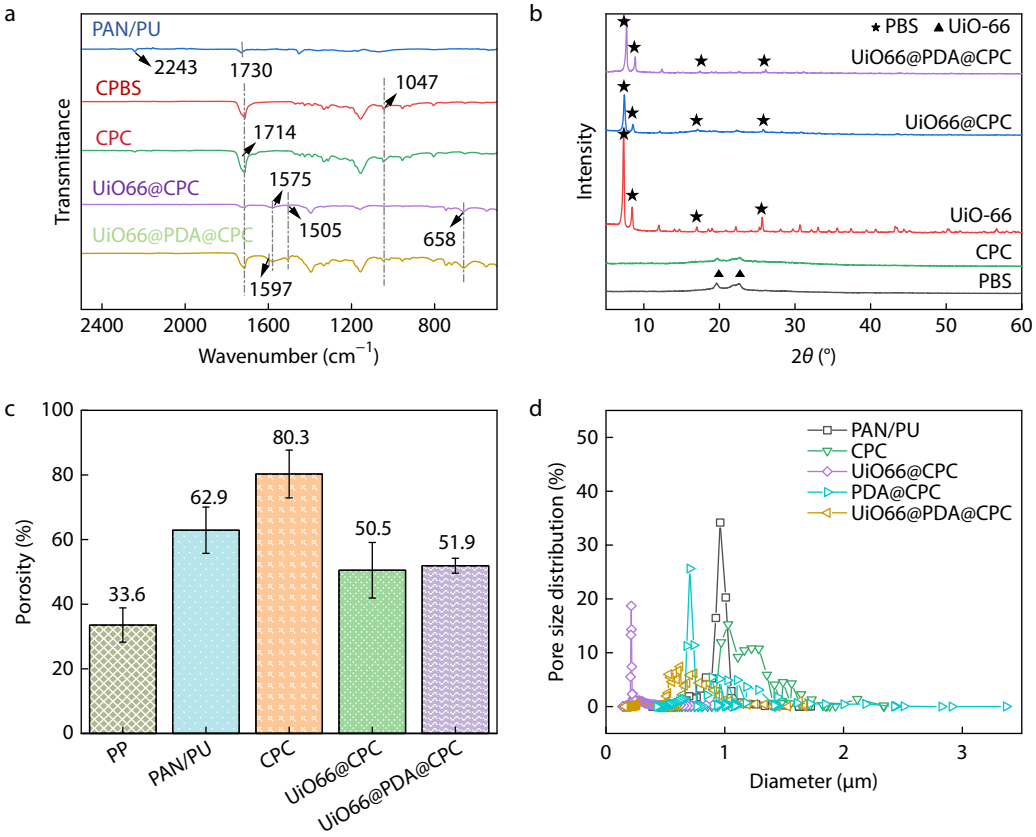

Fig. 4 (a) Infrared spectra, (b) XRD patterns, (c) porosity, and (d) pore size distribution of different ENSs.

porosity helps reduce the risk of contact between the positive and negative electrodes, ensuring the safety of LIBs.

In addition, the pore size distribution of separators plays a crucial role in ion transport. The separator must possess an optimized pore structure to provide efficient transport pathways for Li^+ during charging and discharging while effectively regulating the ion flux distribution to ensure the efficient operation of LIBs.[33] Fig. 4(d) and Table S4 (in ESI) present the pore size distributions of different ENSs. It is evident that the average pore sizes of the UiO66@CPC ENS (0.87) and PDA@CPC ENS (0.75) were smaller than those of the CPC ENS (1.23), while the average pore size of UiO66@PDA@CPC ENS (0.63) further decreased. This reduction stemmed from the polymerization of PDA or the loading of UiO-66 onto the CPC ENS. Meanwhile, compared to CPC ENS (2222/cm^2), the pore count of PDA@CPC ENS (8705/cm^2) was significantly increased, which was due to the rough microporous morphology of the PDA coating and the new smaller pores generated during the process of PDA wrapping the fibers (Fig. 3e). After loading UiO-66, the decrease in the pore count in UiO66@PDA@CPC ENS (5017/cm^2) was due to UiO-66 filling some gaps. Notably, compared to UiO66@CPC ENS (0.23–3.14 μm), the filling process of UiO-66 was uniform due to the PDA layer, resulting in the narrowest pore size distribution of UiO66@PDA@CPC ENS (0.44–1.67 μm), indicating its most uniform pore distribution. Accordingly, the UiO66@PDA@CPC ENS exhibited a suitable pore size distribution, with the smallest pore size and the most uniform pore distribution (Table S4 in ESI), which was crucial for enhancing the long-term Li^+ transport efficiency. Furthermore, the higher number of pores facilitates the smooth passage of ions, reducing the likelihood of lithium dendrites piercing the separator, thereby improving the safety and long-term stability of LIBs.

Electrolyte Affinity and Mechanical Properties of ENSs

The electrolyte affinity of the separators is also a key factor influencing their electrochemical performance, which is typically characterized by the wettability and uptake rate of the separator to the electrolyte. Superior wettability ensures uniform distribution of the electrolyte across the separator, facilitating efficient ion transport. As shown in Fig. 5(a), all ENSs exhibited contact angles smaller than that of PP (45.1°±0.4°), indicating enhanced electrolyte wetting and diffusion within the ENSs because of the three-dimensional network structure of the ENSs. The UiO66@PDA@CPC ENS exhibited the smallest electrolyte contact angle, demonstrating its superior electrolyte wettability. This was attributed not only to its high porosity, which facilitated rapid electrolyte penetration, but also to the introduction of UiO-66 with a porous structure and rich polar groups, which further promoted rapid electrolyte diffusion.

The electrolyte uptake rate of the separators was closely related to the porosity and polar groups contained in the separators. Separators with high electrolyte uptake rates can maintain a stable performance over extended periods, enabling LIBs to achieve efficient and long-lasting operation. As shown in Fig. 5(b), the electrolyte uptake rates of all ENSs were higher than that of the PP separator (76.1%±8.8%) owing to their superior porosity and pore structure. UiO66@CPC

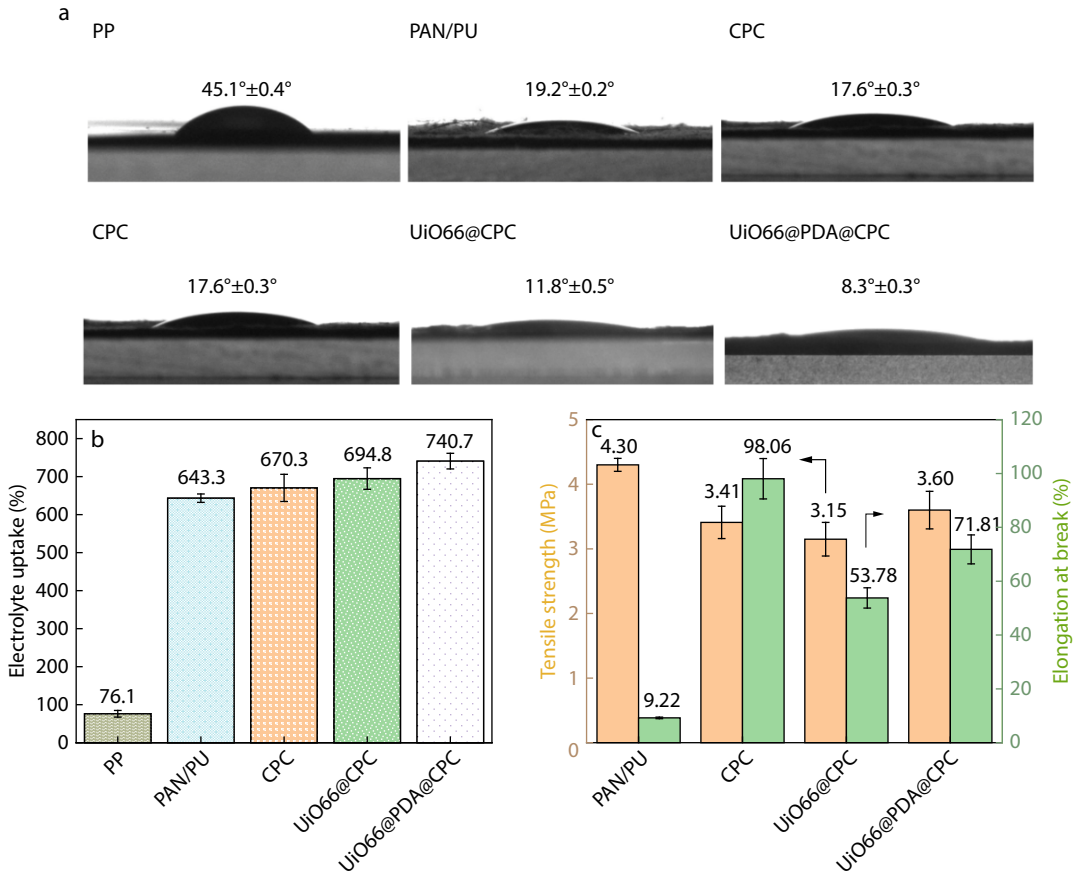

Fig. 5 (a) Electrolyte wettability, (b) electrolyte uptake rate and (c) mechanical properties of different separators.

and UiO66@PDA@CPC ENSs exhibited excellent electrolyte uptake rates of 694.8%±28.3% and 740.7%±20.6%, respectively, which were higher than that of CPC ENS (670.3%±35.8%). This was because the polar groups of PDA and UiO-66 conferred superior electrolyte wettability, which played a crucial role in enhancing electrolyte affinity. The superior electrolyte affinity of the UiO66@PDA@CPC ENS not only helped reduce its interfacial impedance, but also improved its ionic conductivity, resulting in outstanding electrochemical performance.

Fig. 5(c) shows the tensile strength and elongation at break of different ENSs. After the composite of PAN/PU and CPBS ENSs, the elongation at break of the CPC ENS increased to 98.06%±7.50%, which was much higher than that of PAN-2 (9.22%±0.29%). However, the elongation at break of UiO66@CPC and UiO66@PDA@CPC ENSs was lower than that of CPC ENS, which might be related to the introduction of UiO-66 particles partially impairing the uniformity of ENS, leading to excessive local stress during testing, thereby reducing the toughness of ENS. Notably, the tensile strength and elongation at break of UiO66@PDA@CPC ENS were (3.60±0.29) MPa and 71.81%±5.40%, respectively, both higher than those of UiO66@CPC ENS (3.15±0.26 MPa and 53.78%±3.80%). This might be due to the relatively uneven distribution of UiO-66 in the UiO66@CPC ENS, where UiO-66 aggregates tended to become stress concentration points, thereby reducing its mechanical properties. Additionally, the superior mechanical properties of the UiO66@PDA@CPC ENS compared to those of the UiO66@CPC ENS might also be attributed to the strong adhesive PDA shell formed on its surface. This shell layer created additional cross-linking points between fibers, thereby enhancing inter-fiber interactions and improving the overall mechanical properties of the three-layer ENS.[34]

Thermal Properties and Self-closing Function

The thermal stability of the separators is another critical factor affecting battery safety. Contraction, deformation, or melting of the separator at high temperatures can cause direct contact between the positive and negative electrodes of the battery, leading to more severe thermal runaway and even explosions, resulting in serious safety incidents.[32] Fig. 6(a) shows photographs of the PP separator and different ENSs after they were placed at different temperatures for 30 min. It can be seen that the CPC ENS underwent significant thermal shrinkage at 85 °C, and this phenomenon became more pronounced as the temperature increased to 100 °C. This indicated that the presence of PBS made CPC ENSs more prone to shrinkage owing to the lower melting point of PBS. However, when the temperature was increased to 140 and 160 °C, the size of the CPC ENS did not undergo significant changes, which might be related to the preservation of a certain framework by the PAN/PU layer with high thermal stability in the three-layer ENS. Additionally, the PP separator lost its original shape at 160 °C, whereas the PAN/PU, UiO66@CPC, and UiO66@PDA@CPC ENSs maintained their initial size without obvious changes. This is because the excellent

https://doi.org/10.1007/s10118-026-3772-9

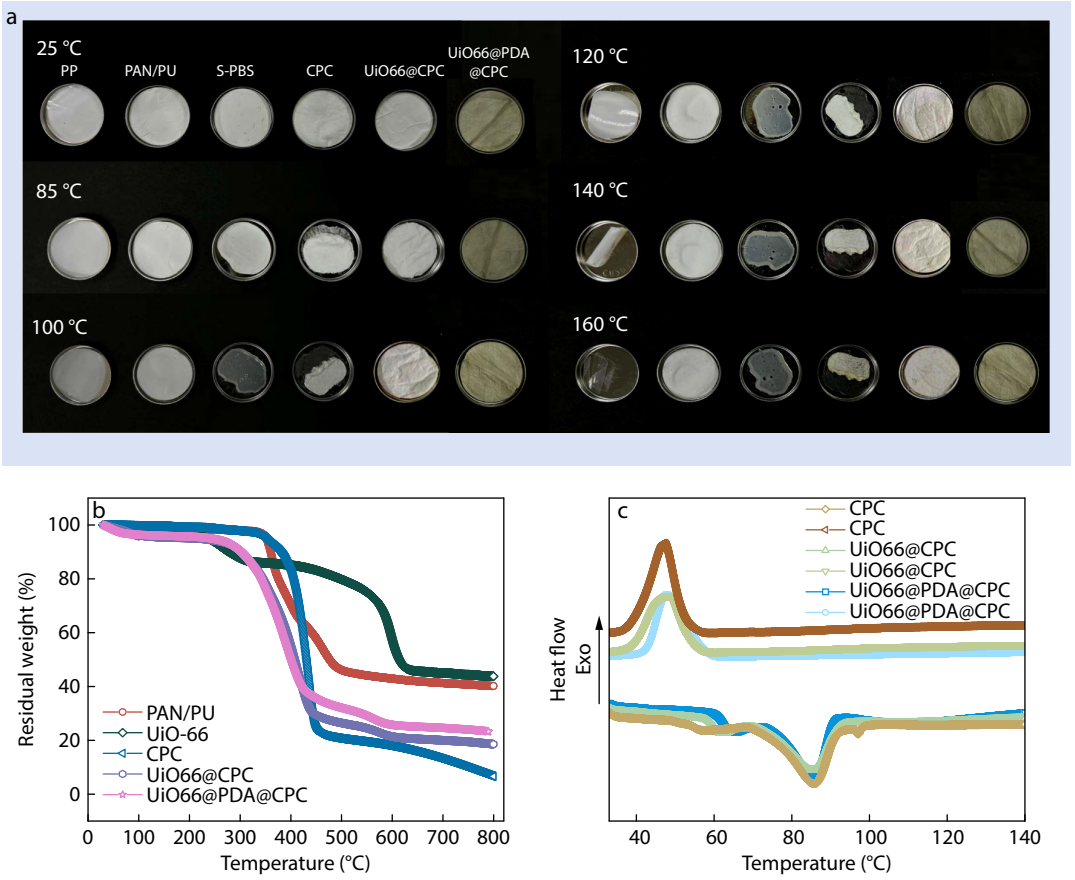

Fig. 6 (a) Thermal shrinkage performance of different ENSs, (b) TG thermograms of different samples and (c) DSC curves of different three-layer ENSs.

high-temperature resistance of UiO-66 and PDA effectively suppressed the shrinkage and deformation of the ENS at high temperatures, maintaining its structural integrity.[35,36]

The thermal properties of the different ENSs were analyzed by TG testing. As shown in Fig. 6(b), PAN/PU began to experience weight loss at approximately 200 °C, likely due to the breakage and decomposition of PU molecular chains in PAN/PU.[37] Within the temperature ranges of 300–350 °C and 350–450 °C, a sharp increase in the weight loss of PAN/PU was observed, which was due to the oligomerization and cyclization of nitrile groups in PAN molecules, as well as the degradation and thermal oxidation reactions of PAN at higher temperatures.[38–40] The CPC ENS also exhibited an initial mild weight loss at approximately 200 °C, similar to the single-layer PAN/PU ENS, followed by a pronounced decrease at approximately 350 °C, corresponding to the decomposition temperature of PBS, which was primarily attributed to the breaking of ester bonds.[41] The weight loss of UiO-66 below 100 °C was due to the desorption of moisture contained in the particles. The weight loss between 100 and 400 °C was primarily caused by the dehydroxylation of $Zr_6O_4(OH)_4$ (from $Zr_6O_4(OH)_4$ to Zr_6O_6). The weight loss between 400 °C and 550 °C corresponds to the second weight loss stage, primarily caused by the transformation from $Zr_6O_4(OH)_4(BDC)_6$ to $6{\cdot}ZrO_2$.[17,42] When the heating temperature approached 490 °C, the weight of the PP separator decreased sharply, with its residual weight approaching 0%. At 800 °C, the final residual weights of the PAN/PU, UiO-66, UiO66@CPC ENS, and UiO66@PDA@CPC ENS were 40.18%, 43.79%, 18.56%, and 20.22%, respectively, which were higher than those of the CPC ENS (6.59%), further demonstrating the superior thermal stability of the M-PDA@SCPBS ENS.

DSC is an effective method for determining the thermal-closing performance of separators, and the temperature at which the separator stops working is typically close to the melting temperature. The DSC curves of CPC, UiO66@CPC, and UiO66@PDA@CPC ENSs (Fig. 6c) exhibit a broad exothermic peak at approximately 60 °C, which might be attributed to the desorption of residual solvents (*e.g.*, DMF) or moisture in UiO-66. Meanwhile, a sharp PBS melting peak appeared at 85 °C in all three-layer ENSs, and an exothermic peak caused by the melting of PU soft segments appeared near 100 °C in the CPC ENS.[43] However, the DSC curves of the UiO66@CPC and UiO66@PDA@CPC ENSs did not show this peak because the introduction of UiO-66 further reduced the PU content in the three-layer ENSs. Furthermore, the morphological changes of the ENSs under high-temperature conditions could also effectively determine the thermal-closing status of the ENS. Fig. S4 (in ESI) shows the surface SEM images of CPC, UiO66@CPC, and UiO66@PDA@CPC ENSs after 15 min of heat treatment at 85 °C. It could be seen that the originally porous ENSs had transformed into ENSs with a non-porous structure. Among them, UiO66@CPC and UiO66@PDA@CPC ENSs exhibited only a small number of particles distributed on the sur-

https://doi.org/10.1007/s10118-026-3772-9

face after heat treatment. This was because molten PBS completely blocked the pores of the ENS, restricting ion transport and inhibiting electrochemical reactions, thus effectively preventing thermal runaway in LIBs. Notably, the thermal shutdown behavior at 85 °C was irreversible. Once the low-melting PBS outer layer melts and seals the pores, the original fibrous and porous structure of the ENS cannot be restored, even after cooling.

Electrochemical Performance

A high ionic conductivity facilitates the rapid migration of Li^+ at high current densities and significantly improves the rate performance of LIBs.[44] Fig. 7(a) and Table 1 show that the ionic conductivities of all ENSs exceeded those of the PP separator (0.24 mS/cm), which was attributed to their high porosity, uniformly interconnected pore distribution, high electrolyte uptake rate, and excellent electrolyte wettability.[45] Among them, the ionic conductivity of UiO66@CPC and UiO66@PDA@CPC both exceeded that of CPC ENS because the polar groups in UiO-66 facilitated more electrolyte absorption and storage by the ENS, thereby enhancing its ion transport. However, the bulk resistances of the sandwich-structured CPC, UiO66@CPC, and UiO66@PDA@CPC ENSs all increased sharply after 15 min of heat treatment at 85 °C, reaching 175.7, 746.9, and 908.9 Ω, respectively (Fig. 7b). This indicates that ion migration in the batteries was severely hindered at this temperature, making the sandwich-structured ENSs unable to ensure the normal operation of the assembled batteries, suggesting that these ENSs had a self-closing function at 85 °C. Notably, upon heating to 85 °C, molten PBS permanently sealed the pores and fully obstructed the ion transport channels. The residual resistance of the ENSs originated from the thin electrolyte film instead of valid ion conduction across the ENS. The increased resistance after UiO-66 incorporation stemmed from uniform pore closure and strengthened interfacial interaction. Fig. 7(c) shows that the interfacial impedance of the UiO66@PDA@CPC ENS was lower than that of CPC and UiO66@CPC, illustrating that the UiO66@PDA@CPC ENS had better interface compatibility with electrolytes and electrodes, thereby promoting efficient Li^+ migration and further enhancing the electrochemical performance of LIBs. This was primarily attributed to the excellent affinity of UiO66@PDA@CPC ENS for the electrolyte, which effectively accelerated Li^+ transport. Additionally, the low interfacial impedance of the UiO66@PDA@CPC ENS was related to its rela-

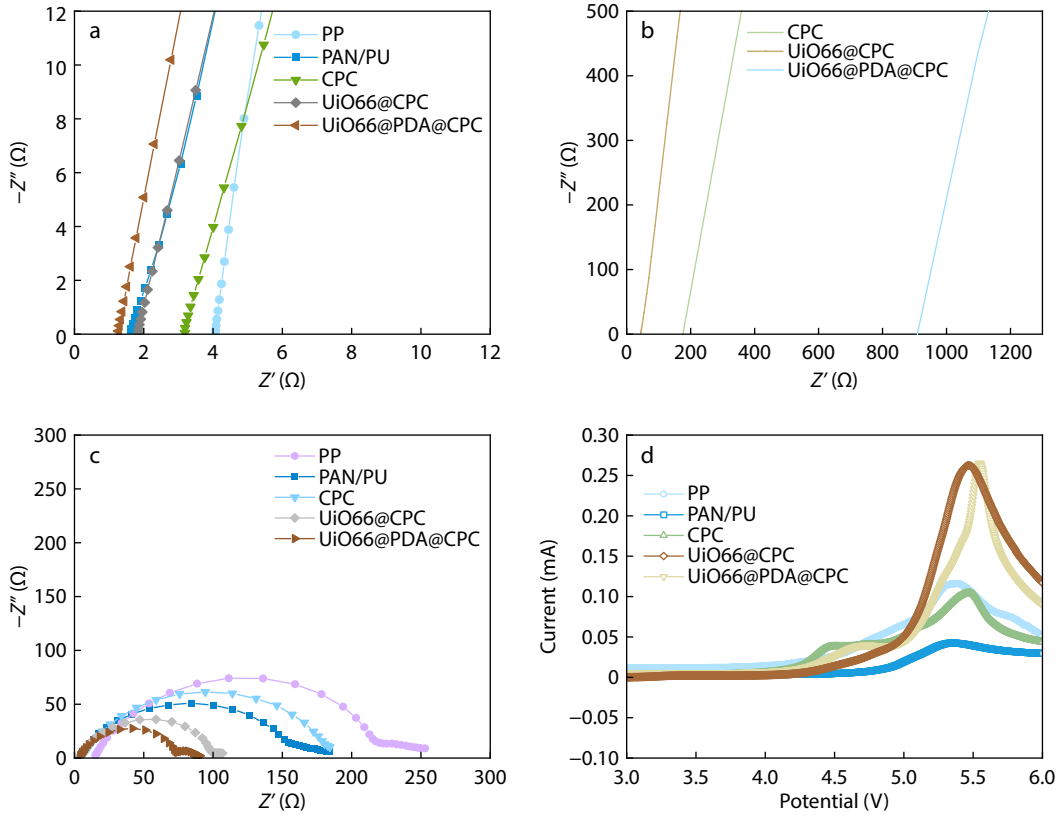

Fig. 7 Ion conductivity of different separators (a) at room temperature and (b) after 15 min of heat treatment at 85 °C; (c) AC impedance plots and (d) LSV curves of batteries assembled with different separators.

Table 1 δ and t_{Li^+} values of three different ENSs.

ENSs	R_b (Ω)	δ (mS/cm)	Thickness (mm)	t_{Li^+}	Interfacial impedance (Ω)
CPC	3.2	2.09	0.170	0.30	197.2
UiO66@CPC	1.8	3.06	0.131	0.53	103.1
UiO66@PDA@CPC	1.3	3.35	0.120	0.63	74.4

tively uniform pore structure and outstanding electrolyte uptake rate.

During the charge-discharge cycles of LIBs, the separator must maintain electrochemical stability to prevent redox reactions from disrupting the internal chemical environment. LSV tests were performed to investigate the electrochemical stabilities of the separators. As shown in Fig. 7(d), the current values of all batteries remained stable at voltages below 4.2 V, indicating the stable electrochemical performance of the batteries. However, as the voltage increased, the electrochemical stability window of the CPC ENS-assembled battery was 4.8 V, which was similar to that of the PAN/PU (4.9 V) and larger than that of the PP separator (4.3 V). Moreover, the batteries assembled with UiO66@CPC and UiO66@PDA@CPC ENSs possessed a broader electrochemical stability window (5.0 V), ensuring their excellent stability within the operating voltage range of LIBs and enhancing their safety.

The Li^+ transference number in the separators is a critical factor influencing the separator performance. A higher ion transference number indicates a greater Li^+ transport efficiency, signifying an enhanced charge transfer efficiency between the cathode and anode in the electrolyte.[46,47] As shown in Fig. S5 (in ESI) and Table 1, the ionic transference of CPC, UiO66@CPC, and UiO66@PDA@CPC ENSs was calculated from the current-time curves and resistance changes before and after battery polarization. The UiO66@PDA@CPC ENS exhibited the highest ionic transference, and its ion transfer principle is shown in Fig. 8. The surface of the UiO66@PDA@CPC ENS contained a large number of polar groups (*e.g.*, hydroxyl, ester, and other oxygen-containing groups), which could enhance the affinity between the separator surface and the electrolyte, thereby reducing the ion transport resistance. Concurrently, the OMSs incorporated in UiO-66 loaded on the ENS could effectively adsorb anions, facilitating rapid Li^+ migration.

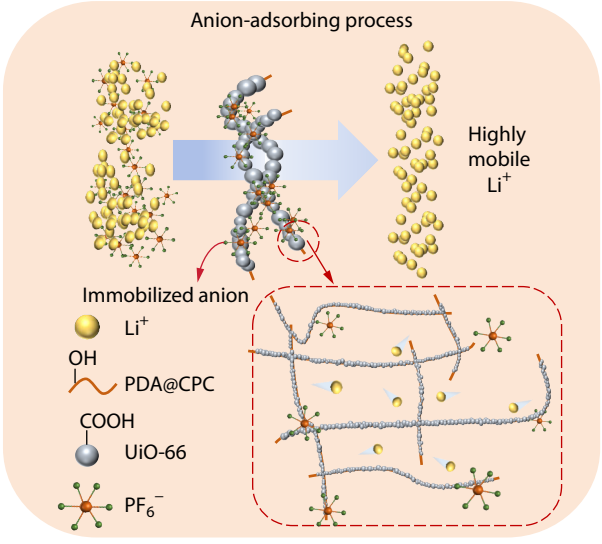

Fig. 8 Schematic diagram of ion migration in UiO66@PDA@CPC ENS assembled batteries.

Cycling and Rate Performance

The cycling and rate performances of LIBs are important indicators for evaluating the practicality of separators. Fig. 9(a) shows the cycling performance of the LIBs assembled with different separators at 0.5 C. It could be found that the battery assembled with UiO66@PDA@CPC ENS demonstrated a high initial discharge specific capacity (151.1 mAh/g), and still maintained a higher discharge specific capacity (139.6 mAh/g) after 100 cycles, with a capacity retention rate of 92.4%. Notably, compared to batteries assembled with other separators, the discharge specific capacity of this battery remained almost stable during cycling. This was attributed to the high porosity and good electrolyte affinity of the UiO66@PDA@CPC ENS, as well as the tight bonding between UiO-66 and the substrate. However, the battery assembled with the UiO66@CPC ENS deteriorated rapidly after 80 cycles, which might be related to the detachment of the UiO-66 particles during cycling.

Fig. 9(b) illustrates that, as the rate increased, the discharge specific capacity of the assembled batteries continuously decreased. However, at the same rate, the battery assembled with UiO66@PDA@CPC ENS exhibited the highest discharge specific capacity and could still maintain the highest discharge specific capacity (125.6 mAh/g) at 2.0 C, which was attributed to its lower interfacial impedance and excellent electrolyte affinity. Furthermore, when the rate was restored from 2.0 C to 0.2 C, the discharge specific capacity of the UiO66@PDA@CPC ENS-assembled battery nearly recovered its initial value, demonstrating its outstanding reversibility. This indicates that it could still maintain good electrochemical performance after multiple charge-discharge cycles at varying rates. Overall, the UiO66@PDA@CPC ENS exhibited favorable cycling stability and rate performance, attributed to their low interfacial impedance, high ionic conductivity, and ion mobility. Compared to the ENSs reported in previous studies,[48–57] the UiO66@PDA@CPC ENS exhibited superior comprehensive electrochemical performance (Table S1 in ESI), indicating its potential as an ideal candidate material for LIB separators.

Fig. 9(c) presents the long-cycle performance of the LIB assembled with the UiO66@PDA@CPC ENS at 0.5 C. It was found that the LIB still maintained a discharge specific capacity of 121.89 mAh/g after 180 cycles, with a capacity retention rate of 80.7%, demonstrating the long-term cycling stability of UiO66@PDA@CPC ENS. In addition, to demonstrate the shutdown behavior of the LIB assembled with UiO66@PDA@CPC ENS, its cycling performance was tested under variable-temperature conditions from room temperature (20 °C) to 85 °C at a heating rate of 10 °C/h, as shown in Fig. 9(d). It could be seen that as the operating temperature increased from 20 °C to 80 °C, the LIB assembled with UiO66@PDA@CPC ENS could operate stably with a capacity retention rate of 99.3%. Once held at a constant 85 °C, the discharge specific capacity of the battery dropped to zero, which further confirmed the thermal self-closing function of the UiO66@PDA@CPC ENS. This was because the CPBS fibers in the outer layer completely melted at 85 °C, which blocked the pore structure of the ENS and impeded Li^+ migration, effectively terminating the electrochemical reaction inside the battery and thus achieving the thermal self-closing function.

Fig. S6 (in ESI) displays the SEM images of the lithium plate surface of batteries assembled with PP separators, CPC ENS,

and UiO66@PDA@CPC ENS after 100 cycles. As shown in Fig. S5(a) (in ESI), the surface of the lithium plate appeared smooth before cycling. However, the lithium plate surface of the battery assembled with the PP separator became uneven after 100 cycles (Fig. S5b in ESI), with many deep holes owing to the uneven deposition and stripping of Li^+ during charging and discharging. Excessive deposition in certain areas and dead lithium formed by lithium dendrite breakage cannot participate in subsequent electrochemical reactions, thereby affecting the cycling performance of the battery.[58] The lithium plate surface of the CPC ENS-assembled battery exhibited a relatively rough morphology after 100 cycles (Fig. S5c in ESI), displaying a scale-like appearance, which is potentially related to uneven Li^+ migration during charging. The lithium plate surface of the UiO66@PDA@CPC ENS-assembled battery exhibited a relatively continuous and flat morphology after 100 cycles (Fig. S5d in ESI). This was attributed to the incorporated UiO-66 capturing anions, enhancing the ionic mobility, which is conducive to the uniform insertion and extraction of Li^+, leading to a uniform Li^+ flux distribution and the promotion of homogeneous metallic lithium deposition, thus effectively mitigating lithium dendrite growth. The mechanism by which the UiO66@PDA@CPC ENS regulates the Li^+ transference number and suppresses lithium dendrites is shown in Fig. 10, indicating its benefits for the safety and long-term stability of LIBs.

To investigate the structural stability of the CPC and UiO66@PDA@CPC ENSs after cycling, their surface morphologies were characterized and analyzed after 100 cycles, as shown in Fig. S7 (in ESI). After 100 cycles, the CPC ENS re-

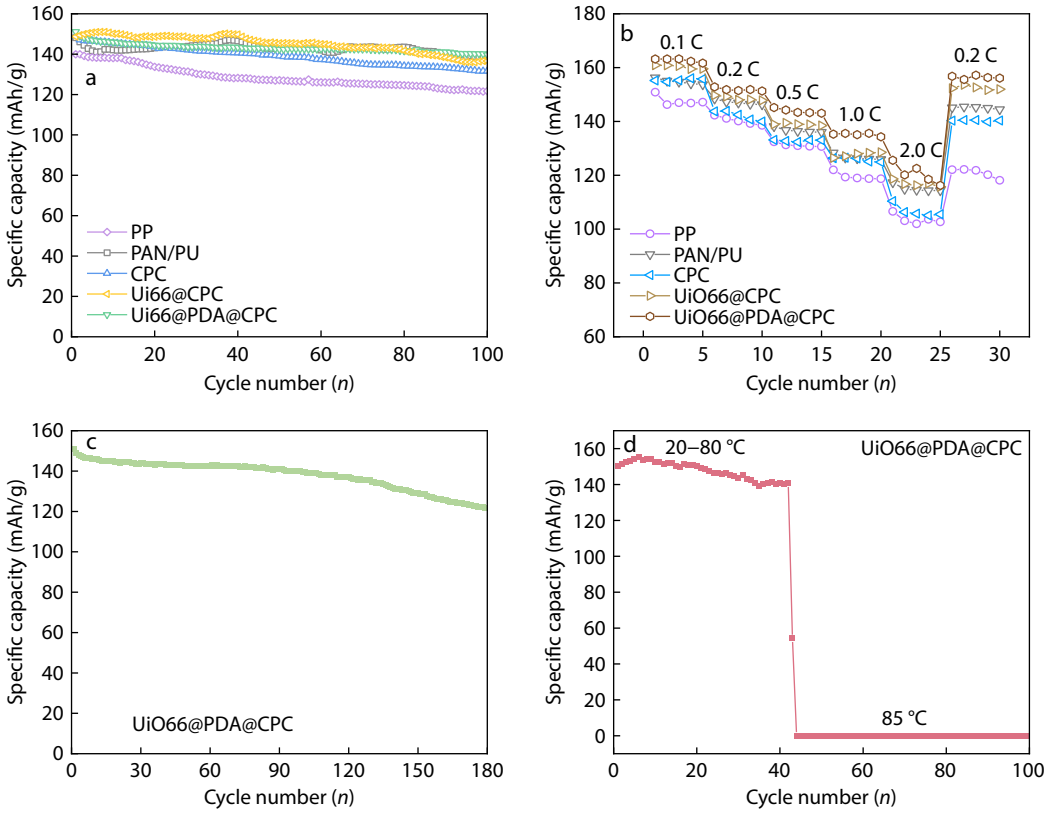

Fig. 9 (a) Cycling stability and (b) rate performance of LIBs assembled with different separators; (c) Long-cycle performance and (d) temperature-dependent cycle performance of LIBs assembled with UiO66@PDA@CPC ENS.

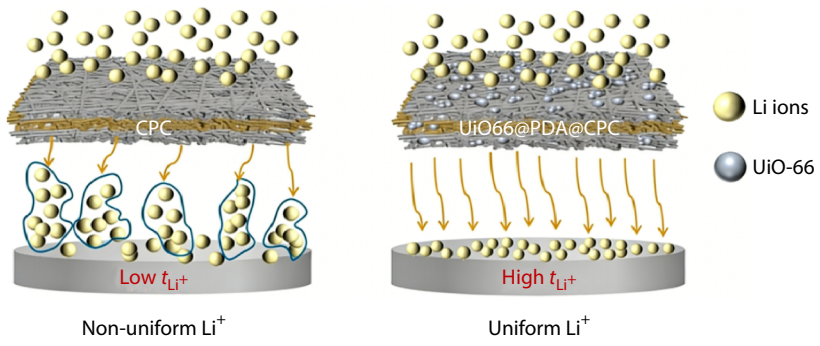

Fig. 10 Mechanism of UiO66@PDA@CPC ENS regulating Li^+ migration and suppressing lithium dendrites.

tained distinct fiber structure features, but there was growth of block-shaped dead lithium on its surface (Fig. S7a in ESI), which was due to the uneven migration of Li^+, leading to excessive local lithium deposition. These dead lithium deposits could clog the pores in the separator, obstructing Li^+ transport and thus affecting LIB performance.[17,24] The UiO66@PDA@CPC ENS retained a well-preserved fibrous morphology after cycling, with only a small amount of dead lithium generated on the surface (Fig. S7b in ESI). More importantly, the porous structure of the ENS remained highly intact, and its network-like pore architecture provided ample pathways for Li^+ transport, further validating the exceptional structural stability of the UiO66@PDA@CPC ENS.

Individual Contributions of Components and Their Synergy

From the perspective of the individual contributions of the components in the UiO66@PDA@CPC ENS, the PAN/PU intermediate layer primarily served as a thermally stable framework, maintaining the mechanical integrity of the separator at temperatures above the melting point of PBS, thereby preventing catastrophic structural collapse. The outer CPBS layers were designed as a thermal-responsive component, which effectively sealed the pore structure by melting at approximately 85 °C, enabling the crucial thermal self-closing function to mitigate thermal runaway. PDA coating plays a pivotal dual role. On the one hand, it significantly enhanced the interfacial adhesion between the fibers, improving the mechanical strength of the ENS. On the other hand, the abundant phenolic hydroxyl groups provided uniform and stable anchoring sites for the subsequent loading of UiO-66 nanoparticles, as evidenced by the morphological comparison between UiO66@CPC ENS and UiO66@PDA@CPC ENS. The loaded UiO-66 nanoparticles served as key functional additives for enhancing the electrochemical performance of ENSs. Their inherent porous structure and OMSs synergistically contributed to superior electrolyte uptake/wettability, facilitated Li^+ transport *via* anion adsorption, and promoted a uniform lithium-ion flux, which collectively suppressed lithium dendrite growth. In summary, the independent functions and synergistic effects of CPC, PDA, and UiO-66 were clearly demonstrated *via* the performance evaluation of CPC, UiO-66@CPC, and UiO-66@PDA@CPC. Owing to its advantages of thermal stability, self-closing performance, wettability, and ion transport, UiO-66@PDA@CPC was verified to be a high-performance and safe separator.

CONCLUSIONS

This study focused on the potential safety hazards of LIBs caused by heat generation during charge-discharge cycles. By selecting the materials and designing the structure of ENSs, SS-FSE technology was used to efficiently prepare sandwich-structured high-temperature self-closing CPC ENSs. In this structure, the PAN/PU middle layer provided excellent thermal stability, while the CPBS outer layer conferred a high-temperature self-closing function, allowing the timely prevention of electrochemical reactions at high temperatures and effectively preventing thermal runaway, thereby improving the safety of LIBs. However, CPC ENS have significant drawbacks in terms of thermal stability and interfacial impedance, and the ion conductivity was not significantly improved, which directly affected the cycling and rate performance of the batteries assembled from them.

To enhance the thermal stability and electrochemical performance of CPC ENS, UiO-66 with a porous structure and abundant active sites was introduced into CPC ENS, and high-performance high-temperature self-closing UiO66@PDA@CPC ENS were successfully prepared. The results indicated that the UiO66@PDA@CPC ENS possessed a uniform and finely porous structure with a high pore count, which contributed to superior electrolyte uptake (740.7%±20.6%) and wettability (8.3°±0.3°). This porous architecture provides ample pathways for Li^+ transport, effectively reduces the interfacial impedance, and enables long-term stable lithium-ion conduction. Meanwhile, the OMSs contained in UiO-66 effectively adsorbed anions, endowing UiO66@PDA@CPC ENS with a high Li^+ transference number (0.63), which reflected excellent electrochemical performance. In addition, the first cycle discharge specific capacity of the battery assembled by it at 0.5 C was 151.1 mAh/g. After 100 cycles, the discharge specific capacity remained 139.6 mAh/g, with a capacity retention rate of 92.4%. The surface of the lithium sheet exhibited a continuous and flat morphology, indicating good long-term cycling stability. Overall, the UiO66@PDA@CPC ENS demonstrated superior electrochemical performance and cycling stability, making it an ideal candidate material for LIB separators.

Conflict of Interests

The authors declare no interest conflict.

Electronic Supplementary Information

Electronic supplementary information (ESI) is available free of charge in the online version of this article at http://doi.org/10.1007/s10118-026-3772-9.

Data Availability Statement

The related data (DOI: 10.57760/sciencedb.40024; CSTR: 31253.11.sciencedb.40024) for this study are publicly available in the Data Repository of China Association for Science and Technology (https://www.scidb.cn/c/cjps). All original experimental data, characterization results, figures and tables associated with this work can be accessed *via* the above permanent link. The data is released under the CC-BY 4.0 license.

ACKNOWLEDGMENTS

This work was financially supported by the National Natural Science Foundation of China (No.11672198), Jiangsu Engineering Research Center of Textile Dyeing and Printing for Energy Conservation (No. 2024-ERC-9011580324), and PAPD (A Project Funded by the Priority Academic Program Development of Jiangsu Higher Education Institutions).

Graphical Abstract

UiO-66-functionalized Sandwich Composite Separators for Improved Performance and Safety of Lithium-ion Batteries

Wen-Fei Ding, Yu-Xing Liu, and Lan Xu

Soochow University; Jiangsu Advanced Textile Engineering Technology Center

A sandwich electrospun separator with a thermal self-closing was fabricated. UiO-66@PDA modification boosts wettability, ionic conductivity, and cycling stability, effectively suppressing lithium dendrites and thermal runaway.

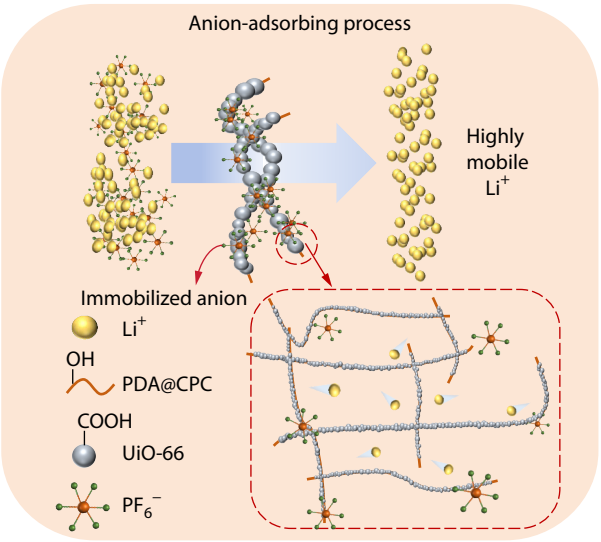

Chinese J. Polym. Sci. 2026 *https://doi.org/10.1007/s10118-026-3772-9*

REFERENCES

1 Biswal, B.; Zhang, B.; Tran, P.; Zhang, J.; Balasubramanian, R. Recycling of spent lithium-ion batteries for a sustainable future: recent advancements. *Chem. Soc. Rev.* **2024**, *53*, 5552–5592.
2 Chen, J.; Asachi, M.; Hassanpour, A.; Babaie, M.; Jabbari, M. Modelling of lithium-ion battery electrode calendering: a critical review. *J. Energy Storage* **2025**, *123*, 116702.
3 Phogat, P.; Dey, S.; Wan, M. Comprehensive review of sodium-ion batteries: principles, materials, performance, challenges, and future perspectives. *Mater. Sci. Eng. B* **2025**, *312*, 117870.
4 Fan, Z.; Chen, X.; Shi, J.; Nie, H.; Zhang, X.; Zhou, X.; Xie, X.; Xue, Z. Functionalized separators boosting electrochemical performances for lithium batteries. *Nano Micro Lett.* **2025**, *17*, 128.
5 Wu, Y.; Wei, W.; Feng, T.; Li, W.; Wang, X.; Wu, T.; Zhang, X. Electrospun MXene/polyimide nanofiber composite separator for enhancing thermal stability and ion transport of lithium-ion batteries. *Front. Chem.* **2025**, *13*, 1555323.
6 Ren, D.; Feng, X.; Liu, L.; Hsu, H.; Lu, L.; Wang, L.; He, X.; Ouyang, M. Investigating the relationship between internal short circuit and thermal runaway of lithium-ion batteries under thermal abuse condition. *Energy Storage Mater.* **2021**, *34*, 563–573.
7 Zhou, G.; Niu, C.; Kong, Y.; Wei, Z.; Wang, J.; Huang, Q.; Lu, H.; Zhang, Q. Research on stimulation responsive electrolytes from the perspective of thermal runaway in lithium-ion batteries: a review. *Fuel* **2024**, *368*, 131599.
8 Ding, W.; Ru, C.; Xu, L. Recent progress in electrospun nanofiber separators for advanced lithium-ion batteries. *J. Energy Storage* **2024**, *102*, 114200.
9 Ding, W.; Xu, L. Batch fabrication of electrospun pan/pu composite separators for safe lithium-ion batteries. *Batteries* **2024**, *10*, 1.
10 Bonakdar, M. A.; Hamdi, O.; Nazarenko, Y.; Ariya, P. A.; Rodrigue, D. Highly porous biobased membranes *via* electrospinning of PBS and CTAB. *Polymer* **2023**, *280*, 126045.
11 Chen, Z.; Yin, X.; Chen, H.; Fu, X.; Sun, Y.; Chen, Q.; Liu, W.; Shen, X. Mechanical, crystallization, rheological, and supercritical CO_2 foaming properties of polybutylene succinate nanocomposites: impact of carbon nanofiber content. *Polymers* **2024**, *16*, 28.
12 Wei, Z.; Gu, J.; Zhang, F.; Pan, Z.; Zhao, Y. Core–shell structured nanofibers for lithium ion battery separator with wide shutdown temperature window and stable electrochemical performance. *ACS Appl. Polym. Mater.* **2020**, *2*, 1989–1996.
13 Coverdale, B. D. M.; Gough, J. E.; Sampson, W. W.; Hoyland, J. A. Use of lecithin to control fiber morphology in electrospun poly (ε-caprolactone) scaffolds for improved tissue engineering applications. *J. Biomed. Mater. Res. Part A* **2017**, *105*, 2865–2874.
14 Bonakdar, M. A.; Kazemi, H.; Rodrigue, D. Conductive and auxetic composite membranes based on graphene nanoplatelets and polybutylene succinate produced *via* electrospinning. *Polym. Eng. Sci.* **2024**, *64*, 1083–1095.
15 Surat'man, N. E. B.; Quek, X. L.; Wang, N.; Ye, E.; Xu, J.; Li, Z.; Li, B. Sustainable nanofibrous membranes for air filtration, water purification and oil removal. *Nanoscale* **2025**, *17*, 6427–6447.
16 Guo, J.; Wang, X.; Shi, L.; Liu, Z. Significantly promoting the lithium-ion transport performances of MOFs-based electrolytes *via* a strategy of introducing fluoro groups in the crystal frameworks. *Chem. Commun.* **2025**, *61*, 2103–2106.
17 Xu, G.; Chen, T.; Zhang, H.; Yin, J.; Qian, Y.; Xiong, Y.; Hu, K.; Gao, H.; Jiang, H.; Guo, P.; Li, J.; Wang, Y.; Yu, S.; Zhu, H. Enhancing the electrochemical properties of polyethylene oxide solid-state electrolytes based on a small nano-sized UiO-66 metal-organic framework. *J. Power Sources* **2024**, *623*, 235512.

18 Li, C.; Xue, P.; Chen, L.; Liu, J.; Wang, Z. Reducing the crystallinity of PEO-based composite electrolyte for high performance lithium batteries. *Compos. Part B Eng.* **2022**, *234*, 109729.
19 Cheng, F.; Qian, J.; Li, H.; Di, J.; He, J.; Bai, Y.; Huang, Y. Polydopamine-assisted *in situ* formation of dense aramid nanofibers layer on polyethylene separator for lithium-ion battery. *J. Appl. Polym. Sci.* **2023**, *140*, e54587.
20 Yang, Z.; Liu, H.; Zhao, J.; Wang, C.; Li, H.; Wang, X.; Yang, Y.; Wu, H.; Gu, Z.; Li, Y. UV absorption enhanced polydopamine coating. *Mater. Horiz.* **2024**, *11*, 2438–2448.
21 Zhang, W.; Zhao, X.; Ma, W. Metal-organic framework/Ti_2VC_2Tx@polydopamine (PDA) derived functional nanostructures for lithium-ion batteries with ultra-high stability at low temperatures. *Diam. Relat. Mater.* **2025**, *159*, 112818.
22 Zhang, S.-S. A review on the separators of liquid electrolyte Li-ion batteries. *J. Power Sources* **2007**, *164*, 351–364.
23 Zhang, J.; Liu, Z.; Kong, Q.; Zhang, C.; Pang, S.; Yue, L.; Wang, X.; Yao, J.; Cui, G. Renewable and superior thermal-resistant cellulose-based composite nonwoven as lithium-ion battery separator. *ACS Appl. Mater. Interfaces* **2013**, *5*, 128–134.
24 Gao, L.; Ding, W.; Xu, L. Batch fabrication and characterization of aligned PAN-based nanofiber membranes for lithium-ion battery separators. *J. Energy Storage* **2024**, *79*, 110230.
25 Pamuła, E.; Błażewicz, M.; Paluszkiewicz, C.; Dobrzyński, P. FTIR study of degradation products of aliphatic polyesters–carbon fibres composites. *J. Mol. Struct.* **2001**, *596*, 69–75.
26 Kim, H.-S.; Kim, H.-J.; Lee, J.-W.; Choi, I.-G. Biodegradability of bio-flour filled biodegradable poly (butylene succinate) bio-composites in natural and compost soil. *Polym. Degrad. Stab.* **2006**, *91*, 1117–1127.
27 Ghasemi, S.; Esmaeili, M.; Dinari, M.; Dabiri, A.; Karbasi, S. UiO-66 metal-organic framework (MOF) as an osteogenic stimulant in the poly-3-hydroxybutyrate-zein/UiO-66 electrospun composite scaffold for bone tissue engineering applications. *J. Polym. Environ.* **2025**, *33*, 2001–2028.
28 Pan, R.; Wang, Z.; Sun, R.; Lindh, J.; Edström, K.; Strømme, M.; Nyholm, L. Polydopamine-based redox-active separators for lithium-ion batteries. *J. Materiomics* **2019**, *5*, 204–213.
29 Yan, K.; Xu, L.; Ahmed, A. PVDF/Fe_3O_4@pDA@Ag nanofiber membranes with multicore–shell structure for EMI shielding. *ACS Appl. Polym. Mater.* **2024**, *6*, 9200–9208.
30 Strauss, I.; Chakarova, K.; Mundstock, A.; Mihaylov, M.; Hadjiivanov, K.; Guschanski, N.; Caro, J. UiO-66 and UiO-66-NH2 based sensors: dielectric and FTIR investigations on the effect of CO_2 adsorption. *Micropor. Mesopor. Mater.* **2020**, *302*, 110227.
31 Dvorackova, M.; Svoboda, P.; Kostka, L.; Pekarova, S. Influence of biodegradation in thermophilic anaerobic aqueous conditions on crystallization of poly(butylene succinate). *Polym. Test.* **2015**, *47*, 59–70.
32 Liu, W.; Lee, S. W.; Lin, D.; Shi, F.; Wang, S.; Sendek, A. D.; Cui, Y. Enhancing ionic conductivity in composite polymer electrolytes with well-aligned ceramic nanowires. *Nat. Energy* **2017**, *2*, 17035.
33 Wu, X. W.; Seenivasan, M.; Karuppiah, C.; Zhang, B. R.; Shih, J. Y.; James Li, Y. J.; Hung, T. F.; Chien, W. C.; Ramaraj, S. K.; Jose, R.; Yang, C. C. Fabrication electro-spun Poly (vinyl alcohol)-Melamine nonwoven membrane composite separator for high-power lithium-ion batteries. *Heliyon* **2024**, *10*, e34436.
34 Wei, Q.; Achazi, K.; Liebe, H.; Schulz, A.; Noeske, P. M.; Grunwald, I.; Haag, R. Mussel-inspired dendritic polymers as universal multifunctional coatings. *Angew. Chem. Int. Ed.* **2014**, *53*, 11650–11655.
35 Perfecto-Irigaray, M.; Beobide, G.; Castillo, O.; da Silva, I.; García-Lojo, D.; Luque, A.; Mendia, A.; Pérez-Yáñez, S. $Zr_6O_4(OH)_4$(benzene-1,4-dicarboxylato)$_6]_n$: a hexagonal polymorph of UiO-66. *Chem. Commun.* **2019**, *55*, 5954–5957.
36 Zhang, Y.; Meng, R.; Zhou, J.; Liu, X.; Guo, W. Halloysite nanotubes-decorated electrospun biobased polyamide scaffolds for tissue engineering applications. *Colloids Surf. A Physicochem. Eng. Aspects* **2022**, *648*, 129378.
37 Bordes, P.; Pollet, E.; Averous, L. Nano-biocomposites: biodegradable polyester/nanoclay systems. *Prog. Polym. Sci.* **2009**, *34*, 125–155.
38 Surianarayanan, M.; Vijayaraghavan, R.; Raghavan, K. V. Spectroscopic investigations of polyacrylonitrile thermal degradation. *J. Polym. Sci. A Polym. Chem.* **1998**, *36*, 2503–2512.
39 Nataraj, S. K.; Yang, K. S.; Aminabhavi, T. M. Polyacrylonitrile-based nanofibers—a state-of-the-art review. *Prog. Polym. Sci.* **2012**, *37*, 487–513.
40 Pożyczka, K.; Marzantowicz, M.; Dygas, J. R.; Krok, F. Ionic conductivity and lithium transference number of poly (ethylene oxide): LiTFSI system. *Electrochim. Acta* **2017**, *227*, 127–135.
41 Oblak, P.; Gonzalez-Gutierrez, J.; Zupančič, B.; Aulova, A.; Emri, I. Processability and mechanical properties of extensively recycled high density polyethylene. *Polym. Degrad. Stab.* **2015**, *114*, 133–145.
42 Tang, X.; Li, J.; Li, J.; Zha, F.; Guo, X.; Tian, H. Peroxidation of methyl ethyl ketone catalyzed by UiO-66 and the thermal stability analysis. *Inorg. Chem. Commun.* **2024**, *170*, 113474.
43 Sirisathitkul, C.; Pholnak, C.; Chareonsuk, T.; Panchawirat, P.; Rugmai, S. Comparative SAXS, DSC and FT-IR spectra of polyurethane coatings filled with hexagonal and sword-like zinc oxide. *Arab. J. Sci. Eng.* **2016**, *41*, 2339–2344.
44 Angulakshmi, N.; Stephan, A. M. Electrospun trilayer polymeric membranes as separator for lithium–ion batteries. *Electrochim. Acta* **2014**, *127*, 167–172.
45 Wang, L.; Wang, Z.; Sun, Y.; Liang, X.; Xiang, H. Sb_2O_3 modified PVDF-CTFE electrospun fibrous membrane as a safe lithium-ion battery separator. *J. Membr. Sci.* **2019**, *572*, 512–519.
46 Ding, L.; Yan, N.; Zhang, S.; Xu, R.; Wu, T.; Yang, F.; Cao, Y.; Xiang, M. Separator impregnated with polyvinyl alcohol to simultaneously improve electrochemical performances and compression resistance. *Electrochim. Acta* **2022**, *403*, 139568.
47 Zhou, Y. G.; Fan, L.; Li, H. Q.; Cui, Y. J.; Yu, S. F.; Wei, Z. Z.; Zhao, Y. Fibrous separator with surface modification and micro-nano fibers lamination enabling fast ion transport for lithium-ion batteries. *Chinese J. Polym. Sci.* **2023**, *41*, 222–232.
48 Yang, K.; Sheng, L.; Zhu, D.; Wang, X.; Tang, Z.; Chen, J.; Chen, R.; Deng, J.; Wang, J.; Tang, Y.; He, X.; Xu, H. Uniform Poly (vinyl ethylene carbonate) based metal-organic framework separator for smooth lithium-ion electrodeposition. *J. Power Sources* **2024**, *624*, 235553.
49 Jiang, Y.; Sun, C.; Dong, F.; Xie, H.; Sun, L. Multilayer polyethylene separator with enhanced thermal properties for safe lithium-ion batteries. *Particuology* **2024**, *91*, 29–37.
50 Chen, Y.; Qiu, L.; Ma, X.; Dong, L.; Jin, Z.; Xia, G.; Du, P.; Xiong, J. Electrospun cellulose polymer nanofiber membrane with flame resistance properties for lithium-ion batteries. *Carbohydr. Polym.* **2020**, *234*, 115907.
51 Deng, J. H.; Cao, D. Q.; Li, L. J.; Chen, Y. P.; Zhang, G. Q.; Yang, X. Q. Electrospun nanofiber separator derived from nano-SiO_2-modified polyimide with superior mechanical flexibility for high-performance lithium-ion battery. *J. Mater. Sci.* **2021**, *56*, 15215–15228.
52 Guo, M.; Zhu, H.; Wan, P.; Xu, F.; Wang, C.; Lu, S.; Zhang, Y.; Fan, H.; Xu, J. Freestanding and ultra-flexible PAN/ZIF-67 hybrid membrane with controlled porosity for high-performance and high-safety lithium batteries separator. *Adv. Fiber Mater.* **2022**, *4*, 1511–1524.
53 Min, Y.; Liu, X.; Guo, L.; Wu, A.; Xian, D.; Zhang, B.; Wang, L. Construction of diversified ion channels in lithium-ion battery

separator using polybenzimidazole and ion-modified metal–organic framework. *ACS Appl. Energy Mater.* **2022**, *5*, 9131−9140.
54 Huang, H.; Yu, B.; Wang, X. A high thermal stable pre-oxidized polyacrylonitrile nanofiber separator for lithium-ion battery. *J. Appl. Polym. Sci.* **2023**, *140*, e54410.
55 Sun, G.; Jiang, S.; Feng, X.; Shi, X.; Zhang, X.; Li, T.; Chen, N.; Hou, L.; Qi, S.; Wu, D. Ultra-robust polyimide nanofiber separators with shutdown function for advanced lithium-ion batteries. *J. Membr. Sci.* **2022**, *645*, 120208.
56 Lu, L.; Gu, J.; Wei, X.; Wei, Z.; Zhao, Y. Nanofibrous composite separator for lithium-ion batteries with high safety. *ACS Appl. Nano Mater.* **2025**, *8*, 3915−3926.
57 Xiao, Y.; Fu, A.; Zou, Y.; Huang, L.; Wang, H.; Su, Y.; Zheng, J. High safety lithium-ion battery enabled by a thermal-induced shutdown separator. *Chem. Eng. J.* **2022**, *438*, 135550.
58 Chen, K.-H.; Wood, K. N.; Kazyak, E.; LePage, W. S.; Davis, A. L.; Sanchez, A. J.; Dasgupta, N. P. Dead lithium: mass transport effects on voltage, capacity, and failure of lithium metal anodes. *J. Mater. Chem. A* **2017**, *5*, 11671−11681.

https://doi.org/10.1007/s10118-026-3772-9